ARTICLE

Check for updates

Coexistence of two types of short-range order in Si–Ge–Sn medium-entropy alloys

Xiaochen Jin [1], Shunda Chen [1] & Tianshu Li [1✉]

Short-range chemical order (SRO) has been shown to play a decisive role in modulating a wide range of physical properties in medium-entropy alloys and high-entropy alloys. The enormous configurational space of these alloys implies multiple forms of SRO may exist, but such structural diversity has not been reported. Here, ab initio-based sampling reveals that Si–Ge–Sn medium-entropy alloys have two distinct forms of SRO, which carry different energies, distinct degrees of local ordering, and dissimilar electronic structures, and co-exist across a wide range of Si–Ge–Sn compositions. We rationalize the co-existence of two SROs through their virtual degeneracy of thermodynamic stability, due to a subtle balance in the change of enthalpy and configurational entropy upon transformation between the two SROs. Such co-existence of SROs suggests an inherent structural heterogeneity, a diffuse electronic structure, and a new route for band engineering in Si–Ge–Sn medium-entropy alloys. More generally, this study indicates possibility of the co-existence of multiple forms of SRO in medium- and high-entropy alloys.

---

[1] Department of Civil and Environmental Engineering, George Washington University, Washington, DC 20052, USA. ✉email: tsli@gwu.edu

A lloys composed of elements with distinct physical and chemical nature often develop a short-range chemical order (SRO), where certain types of elements either attract or repel each other, leading to a distribution of atoms apart from a perfect randomness. Although SRO has been long conceived to exist in alloys[1], the explicit roles of SRO have been identified only recently, including, for example, modulating mechanical properties in metallic alloys[2,3], enhancing thermoelectric figure of merit in semiconducting alloys[4,5], and controlling ion transport in oxide alloys[6]. In particular, very recent breakthrough in atomic-resolution imaging has led to direct observations of SRO in metallic alloys[2,7,8], confirming prior theoretical predictions[9–11], and more importantly, explicitly demonstrating the impact of SRO on alloys' properties.

The development of ordering in random alloys can be rationalized through the energy gain when certain types of neighbors form more (or less) frequently than in a truly random distribution. As a result, an alloy can effectively lower its enthalpy of mixing ΔH_{mix} through adopting an ordering. However, the development of ordering also leads to a deviation from a random distribution, thus lowering configuration entropy of mixing ΔS_{mix}. Therefore, depending on the magnitude of the change in ΔH_{mix} and ΔS_{mix}, three possible scenarios may occur: First, when enthalpy gain due to ordering $|\delta \Delta H_{mix}|$ significantly overweights entropy loss $|-T\delta \Delta S_{mix}|$, alloy strongly favors ordering, and possibly even develops a long-range order (LRO), i.e., formation of compound or intermetallics; Second, when enthalpy grain cannot compensate entropy loss, a random distribution is thermodynamically preferred; Third, when enthalpy gain becomes greater than entropy loss but not by too much, alloy develops a thermodynamic driving force sufficient to favor a local ordering but not enough for a LRO. This is where SRO emerges.

Therefore, the occurrence of SRO in an alloy strongly depends on the free energy landscape in alloy's configurational space. For such, some binary alloys can already develop an SRO even though their configurational space is relatively small[7,12,13]. A ternary alloy, particularly a medium-entropy alloy (MEA), has a significantly larger configurational space, and the corresponding free energy landscape becomes much more complex. Accordingly, SRO is expected to be more likely in MEA and high-entropy alloy (HEA)[14–17]. More importantly, the increasing complexity of the free energy landscape may also well indicate SRO can bear more complex forms[18]. Indeed, very recent simulation study[19] showed the existence of SRO in CoCuFeNiPd HEA can lead to a pseudo-composite microstructure upon mechanical deformation, implying the complexity of SRO. Nevertheless, regardless of the conjecture, it is unclear whether SRO itself can explicitly exhibit structurally distinct forms, which, despite their unique local environment, may co-exist in one alloy.

Here we investigate the SRO behaviors in Si-Ge-Sn MEA alloys that have attracted a substantial interest as potential candidates for mid-infrared photonics owing to their tunable band gap, low-cost, and Si-compatility[20–32]. Although group IV alloys have been commonly conceived as random solid solutions, our recent studies showed both GeSn[12] and SiSn[13] binary alloys exhibit substantial SRO behaviors, albeit with different forms. A natural question is how the SROs from GeSn and SiSn binary alloys would interact each other upon the-formation of a Si-Ge-Sn ternary alloy. Through extensive ab initio-based Monte Carlo (MC)sampling studies involving > 1 million density functional theory (DFT) calculations, here we demonstrate the mixing of GeSn and SiSn binary alloys creates an entirely new landscape of structures in Si-Ge-Sn ternary alloys that cannot be expected through a superposition of the structures from their constituent sub-alloys. In particular, we find that Si-Ge-Sn MEAs canexhibit two distinct types of SROs,

including a new structure of SRO that neither resembles the ones identified in the binary alloys, nor any known stable phases of Si-Ge-Sn. Remarkably, the two types of SROs are found to display drastically different electronic structures but can co-exist in the same Si-Ge-Sn alloys. Through explicitly examining the free energy of Si-Ge-Sn MEA, we rationalize the co-existence through confirming the virtual degeneracy of the thermodynamic stability for the two types of SROs.

Results

Energy landscape and structures of two types of SROs. A few theoretical approaches are available to explore SRO of an alloy, including mean-field methods, e.g., coherent-potential approximation, and explicit many-body approaches, e.g., cluster expansion. Here we employ Metropolis Monte Carlo method combined with Density Functional Theory (MC/DFT) to account for both the needed level of accuracy for differentiating two types of SROs (<9 meV/atom, as shown below) and the local relaxation effect which was proven critical to SRO in GeSn and SiSn alloy systems[13]. Indeed, MC/DFT approach has been successfully applied to investigate SRO in a variety of alloys[9,11–13,33]. An important point that should be taken into consideration when applying MC/DFT is the significant configurational space of a MEA alloy. To ensure sufficient sampling, for each alloy composition, we carry out 5–8 independent MC sampling studies, each of which consists of 15,000–20,000 MC moves starting from different initial random configurations. This leads to a level of sampling ~2000 moves per atom, and a total number of over 1 million DFT calculations for the entire investigated composition domain.

The large-scale MC/DFT study identifies the complex energy landscape of Si–Ge–Sn MEA alloy. As shown in Fig. 1a, the energy of $Si_{0.125}Ge_{0.625}Sn_{0.25}$ is found to rapidly decrease at the initial stage for all the 8 MC samplings. Such decrease in energy is usually indicative of the existence of an SRO, because rearranging atomic configurations leads to optimized structures which are energetically preferred over a random alloy structure. Indeed, similar behaviors were shown in the alloys previously identified to contain SRO[9,11–13,19]. Intriguingly, the MC sampling is then found to converge into two energy levels, in contrast to the single energy level reported in the prior studies[9,11–13,19]. The two energy levels, denoted by high-energy basin and low-energy basin, respectively, are both well below the average energy of a random alloy, but are separated from each other by about 0.6 eV, as shown in Fig. 1a, c. We note that this energy difference (~9 meV/atom) is much greater than the typical magnitude of energy variation due to thermal fluctuation at room temperature (~2 meV/atom) for a 64-atom cell[34].

The large energy difference between the two energy basins may thus well indicate a distinction in the structures associated with the two energy basins. To examine the structural origin, we examine the statistics of all the six types of first nearest neighbors in $Si_{0.125}Ge_{0.625}Sn_{0.25}$, namely, Si–Si, Si–Ge, Si–Sn, Ge–Ge, Ge–Sn, and Sn–Sn. Fig. 1b shows the variation of the instantaneous count of each type of pairs closely follows the variation of energy along the MC trajectory, thus confirming the strong correlation between energy and structure. Importantly, the two energy basins are found to correspond to two distinct combinations of bond counts, respectively, indicating two different types of SROs in Si–Ge–Sn alloy.

To understand the nature of the two types of SROs, we sample in both energy basins and compute the corresponding average tetrahedral structures around a center atom and the SRO parameter α_{ij}^m for the pair between element i and j (see "Methods" for its definition). Figure 2a compares the local structural motifs
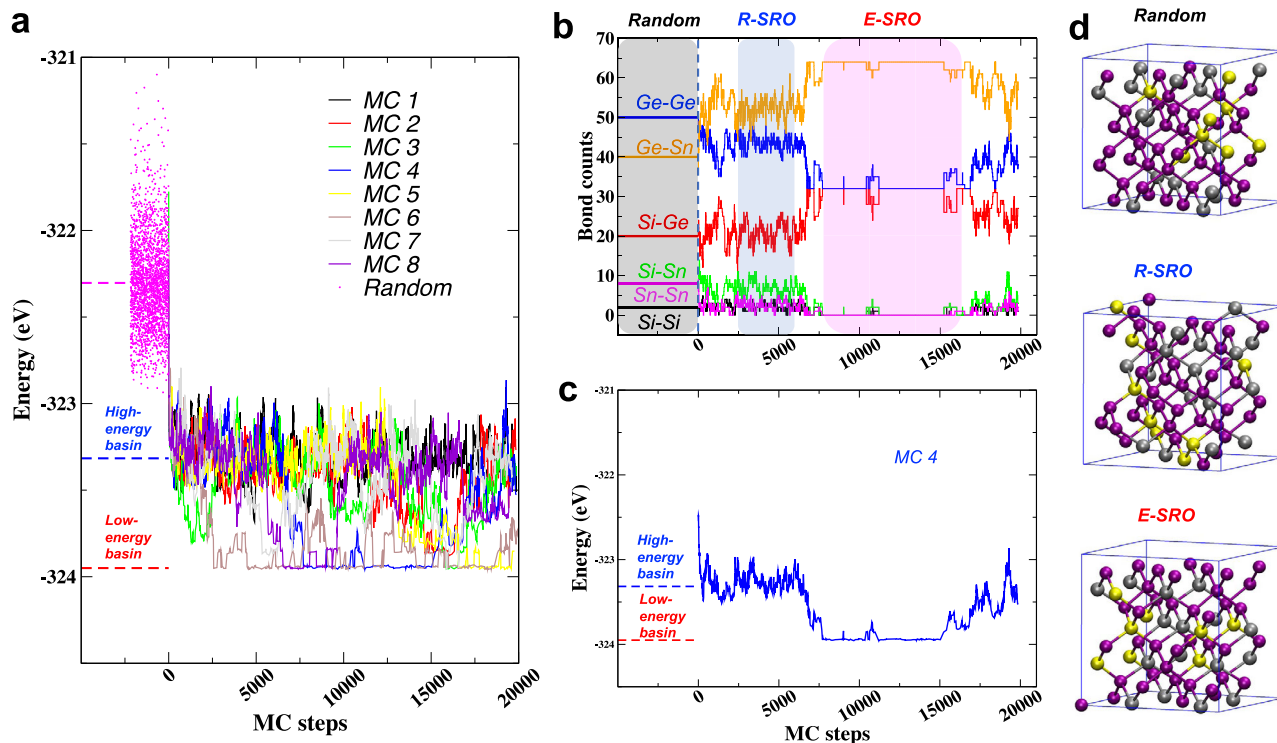
Fig. 1 Variation of energy and structure due to different types of SROs in $Si_{0.125}Ge_{0.625}Sn_{0.25}$. a The overlay of eight independent MC/DFT trajectories shows the total energy fluctuates around two well-defined energy levels: the high-energy basin (blue dashed line) and the low-energy basin (red dashed line) that are separated by ~0.6 eV. Both are well below the average energy (magenta dashed line) from random sampling (magenta dots). For clarity, the energy variation of MC 4 is shown separately in (**c**). In accordance, **b** displays the corresponding variation of bond counts for each type of nearest neighbors. For a truly random distribution, the number of each type of bond with a 64-atom cell (denoted by the horizontal solid lines within the gray-shaded area) is determined only by the overall alloy composition. R-SRO leads to a different combination of six types of bonds (blue-shaded area), yielding a deviation from a random distribution, whereas E-SRO (magenta-shaded area) enhances such deviation. **d** The atomic configurations of random, R-SRO, and E-SRO structures obtained from MC 4. Si, Ge, and Sn atoms are represented by yellow, purple, and silver, respectively.

of a truly random alloy with those identified in the two types of SROs. A truly random alloy was modeled by an ensemble of >2000 randomly generated configurations, each of which was created by randomly assigning the constituent elements to each lattice site in accordance with the nominal alloy composition. For a truly random $Si_{0.125}Ge_{0.625}Sn_{0.25}$ alloy, each center atom, regardless of its type, is surrounded by 0.5 Si atoms, 2.5 Ge atoms, and 1 Sn atom on average, as required by the nominal alloy composition. When the configuration energy falls within the high-energy basin, a major change is found to occur around Sn center atoms: a significant portion of Sn–Sn bonds are replaced by Ge–Sn bonds, leading to a Sn–Sn first coordination number substantially lower than that of a random alloy. In comparison, the local configuration around Si atom remains virtually intact. Ge atoms, on the other hand, have a portion of their nearest-neighbor Ge atoms replaced by Sn atoms, as a result of compensating the depletion of Sn–Sn bonds. The resulted SRO parameter for each pair is shown in Fig. 2b, which clearly indicates SRO occurs mainly through the Sn–Sn and Ge–Sn distribution. We note that this overall structural signature is similar to that identified in $Ge_{0.75}Sn_{0.25}$, which is attributed to the Sn–Sn repulsive interaction[12]. Therefore we denote this type of SRO by regular-SRO (R-SRO).

In comparison, when the energy falls within the low-energy basin, all the structural motifs are found to undergo changes with respect to a random alloy. The most prominent change occurs in the first coordination shell of Sn atoms, where all the Si and Sn atoms are found to be replaced by Ge atoms. As a result, each Sn atom is surrounded by 4 Ge atoms. Since this change leads to a

local Sn structure more ordered than that in R-SRO, we denote it by enhanced-SRO (E-SRO). The elimination of Sn–Sn and Si–Sn bonds then yields the corresponding changes in Si and Ge local structures. For Si, the complete depletion of Sn atoms from its first coordination shell means the bond conservation can only be achieved through Si neighboring with more Ge and/or Si atoms. Our analysis shows that in the case of $Si_{0.125}Ge_{0.625}Sn_{0.25}$, this change is mainly achieved through the augmentation of Si–Ge bonds. On the other hand, the increased number of both Ge–Sn and Si–Ge bonds must be balanced by a depletion of Ge–Ge bonds, as required by the conservation of total number of bonds around Ge. Correspondingly, the Ge–Ge coordination number in E-SRO is found to be lower than that of R-SRO. Therefore, all six types of pairs in E-SRO are found to display substantial deviations from the random distribution, with the most significant deviations occurring in Sn–Sn, Si–Sn, and Si–Si pairs, which lead to a severely distorted SRO polygon, as shown in Fig. 2c. We note that E-SRO does not resemble any of the known phases in Si–Ge–Sn ternary system. In particular, no Si–Ge–Sn intermetallic compound is known to exist[35].

Therefore, the overall structural signature of E-SRO in $Si_{0.125}Ge_{0.625}Sn_{0.25}$ can be characterized through the strong repulsive interactions of Sn-Sn and Si-Sn nearest neighbors. The Sn–Sn repulsion has been recently identified in both GeSn and Si–Sn alloy, which was found to yield a substantially low Sn–Sn coordination number in both alloys[12,13]. Our current study suggests that combining GeSn and SiSn binary alloys into a ternary alloy may facilitate a further depletion of Sn–Sn bonds, leading to a nearly complete elimination of Sn-Sn nearest
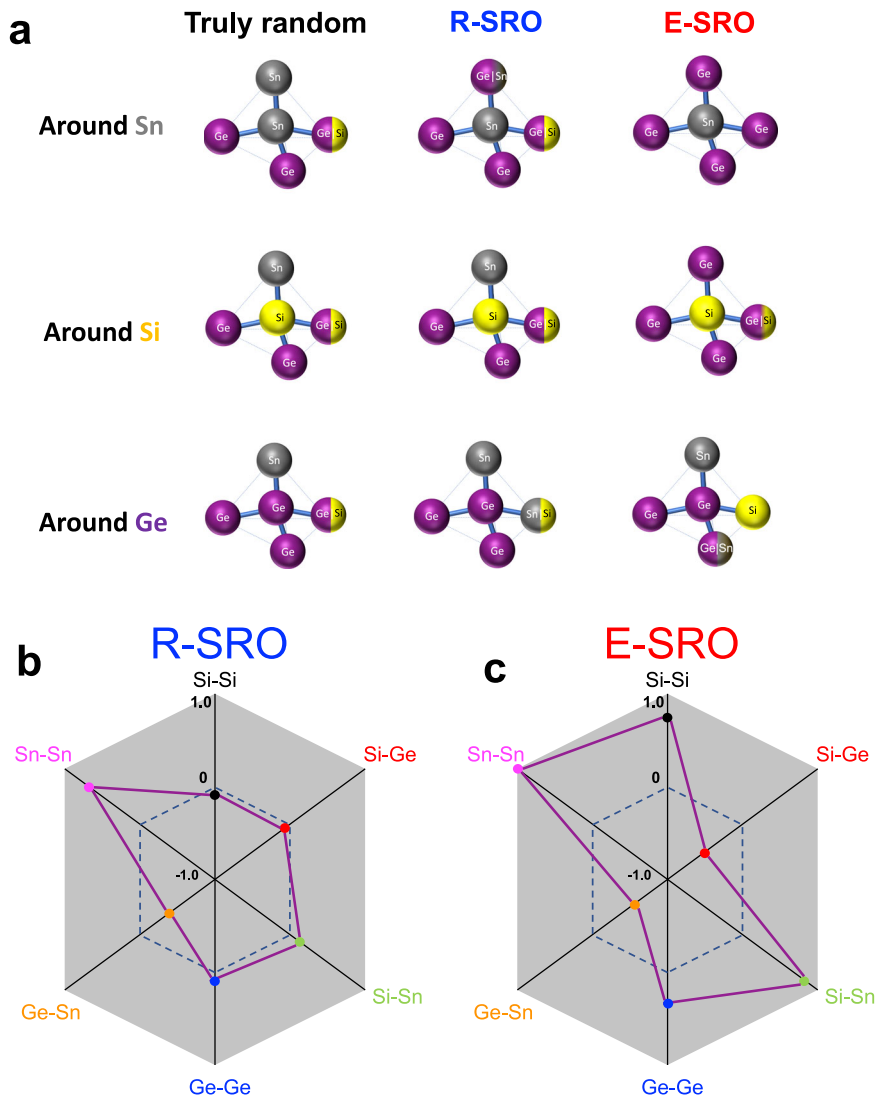
Fig. 2 Structural signatures of R-SRO and E-SRO in Si$_{0.125}$Ge$_{0.625}$Sn$_{0.25}$. a The averaged local tetrahedral structural motif around each alloying element when the alloy adopts a random distribution, R-SRO and E-SRO. **b, c** Show the SRO polygons constructed from the averaged SRO parameter α_{ij}^1 for each type of nearest neighbor in R-SRO and E-SRO, respectively. The averaged SRO parameter α_{ij}^1 for the pair $i - j$ is depicted as a dot on the axis labeled as $i - j$, with its location determined by the value of α_{ij}^1. An SRO polygon (purple solid lines) is obtained through connecting the six dots. The dashed-hexagon represents a random distribution where $\alpha_{ij}^1 = 0$. It is visibly clear that only Ge–Sn and Sn–Sn in R-SRO display substantial deviations from the random distribution, whereas the six types of pairs in E-SRO all show strong non-random distributions.

neighbors in E-SRO. Such a strong Sn–Sn repulsion facilitates a better dispersion of Sn, which works against phase separation. On the other hand, the strong repulsive Si–Sn interaction in E-SRO of Si–Ge–Sn alloys may appear to be at odd with the SRO identified in SiSn alloy[13] at first glance, but we note that such interaction in fact further reduces the number of Sn–Si–Sn local motif, which is the major unfavorable configuration identified in SiSn[13]. Therefore, the E-SRO optimizes the structure of Si–Ge–Sn alloy through reducing all the major unfavorable structures collectively in both GeSn and SiSn sub alloys, which consequently enables a further decrease of configurational energy with respect to R-SRO. It is noted that the structural signatures of both types of SRO are not specific to Si$_{0.125}$Ge$_{0.625}$Sn$_{0.25}$, but rather general in a wide range of compositions, as discussed below and shown in the Supplementary Fig. 2. To this end, we also note that although an explicit experimental characterization of SRO has proved challenging[2,36,37], there do exist evidences suggesting the existence of SRO in Si–Ge–Sn alloy. For example, both atom probe tomography[38] and extended X-ray absorption fine

structure (EXAFS)[39] studies indicated a repulsive interaction between Si and Sn in Si–Ge–Sn alloy, consistent with our finding in E-SRO. In particular, the EXAFS study[39] further showed that Sn atoms prefer to be located at the second nearest neighbor of Sn through a Si–Ge–Sn local bonding structure in Si-Ge-Sn alloys. Consistently, our analysis clearly demonstrates a significant preference of the Si–Ge–Sn triplet local configuration (Fig. 2a and Supplementary Fig. 3) in E-SRO over that in random alloy and R-SRO.

Thermodynamic stability and composition dependence of SROs. An intriguing manifestation of the sampling study is the spontaneous occurrence of both R-SRO and E-SRO, albeit E-SRO clearly being energetically more favorable than R-SRO. In fact, Fig. 1a, c shows the configuration energy fluctuates between the two energy basins in the same trajectories, despite the large difference (0.6 eV) between the two basins. This behavior indicates that both structures contribute to the ensemble average of alloy's
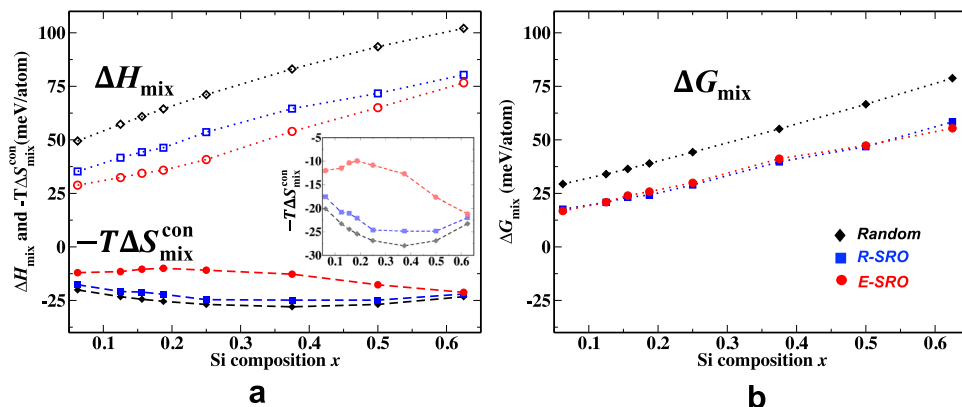
Fig. 3 Thermodynamic analysis of $Si_xGe_{0.75-x}Sn_{0.25}$ alloy at room temperature. a Variation of the calculated enthalpy of mixing ΔH_{mix} (open symbols on the top) and the free energy contribution from the configuration entropy of mixing $-T\Delta S_{mix}^{con}$ (shaded symbols at the bottom) with Si composition x for a random (black), R-SRO (blue) and E-RSO (red). Inset is $-T\Delta S_{mix}^{con}$ at a different scale to show its variation with Si composition. **b** Variation of the calculated total free energy of mixing $\Delta G_{mix} = \Delta H_{mix} - T\Delta S_{mix}^{con}$ with x. R-SRO and E-SRO are nearly degenerate in their ΔG_{mix}.

properties, and more importantly, that R-SRO and E-SRO may have comparable statistical weights towards the ensemble average. The latter can be likely because, although E-SRO is lower in energy, the further ordering of atoms leads to a loss of configurational entropy, which offsets the enthalpy gain. To explicitly examine the thermodynamic stability of Si–Ge–Sn alloy with different SROs, we compute the Gibbs free energy of mixing $\Delta G_{mix} = \Delta H_{mix} - T\Delta S_{mix}^{con}$ for random alloy, R-SRO, and E-SRO. The mixing enthalpy ΔH_{mix}, defined as $H(Si_xGe_{1-x-y}Sn_y) - xH(Si) - (1 - x - y)H(Ge) - yH(Sn)$ for $Si_xGe_{1-x-y}Sn_y$, can be readily calculated through averaging the energy in the corresponding parts of the trajectories from MC sampling (for R-SRO and E-SRO) or from random sampling (for random alloy), while the mixing configurational entropy ΔS_{mix}^{con} is estimated based on the extension to quasi-chemical approximation[40] (see "Methods" for details). As shown in Fig. 3a, the random $Si_{0.125}Ge_{0.625}Sn_{0.25}$ alloy yields an ΔH_{mix} of 57.3 meV/atom, which is reduced to 41.7 meV/atom and 32.4 meV/atom for the R-SRO and E-SRO, respectively. On the other hand, the random alloy leads to the highest configurational entropy of mixing, which, at the room temperature, corresponds to the lowest $-T\Delta S_{mix}^{con}$ of −23.3 meV/atom. Expectedly, SRO is found to raise $-T\Delta S_{mix}^{con}$, through a moderate increase to −20.8 meV/atom via R-SRO and a more significant increase to −11.5 meV/atom via E-SRO. Remarkably, the calculated ΔG_{mix} are found to be nearly identical for R-SRO (20.9 meV/atom) and E-SRO (20.8 meV/atom), which are significantly lower than that of random alloy (34 meV/atom). It is noted that the positive ΔG_{mix} indicates the Si–Ge–Sn alloy is not the thermodynamically stable at room temperature. However, many known phases, including high-Sn content GeSn alloy (with a Sn composition 33 times its equilibrium solubility in Ge)[41], can be grown and stabilized via metastability. More importantly, the virtual degeneracy of ΔG_{mix} between R-SRO and E-SRO thus explains the spontaneous co-occurrence of R-SRO and E-SRO in $Si_{0.125}Ge_{0.625}Sn_{0.25}$ from MC sampling.

The analysis then leads to a question as to whether the co-existence is of a general relevance at other compositions. Obviously, an exhaustive search over the entire compositional space of Si–Ge–Sn alloys can be computationally demanding. In view of the active role of configurational entropy, we address this question by limiting our investigation near the center of the compositional space of the ternary alloy. We also note that this composition range is also of special interest for mid-infrared application (see Supplementary Fig. 4)[42]. For each composition, we carry out 5–8 independent MC/DFT samplings, with a total

number of MC steps comparable to that of $Si_{0.125}Ge_{0.625}Sn_{0.25}$. The sampling study leads to a total of over 1 million DFT calculations (see Supplementary Figs. 5–15). Through this massive sampling study, we identify two types of compositions: namely, the compositions that clearly demonstrate the co-existence of both types of SROs, and those that display the sign of coexistence but have not explicitly exhibited the behavior within the length of the sampling. The compositions explored are indicated in the Si-Ge-Sn pseudo phase diagram, as shown in the Supplementary Fig. 4. From the compositions that show a clear coexistence, we can obtain a meaningful average of energy and structure within the corresponding high- and low-energy basins in the MC trajectories, which enables a similar thermodynamic analysis to compute ΔG_{mix} for R-SRO, E-SRO, and random distribution. The calculation indeed shows the co-existence of two types of SROs is generally associated with the virtual degeneracy of their ΔG_{mix}, as shown in Fig. 3b.

Finally, it is noted that other contributions to ΔG_{mix} also include the vibrational Helmholtz free energy F_{mix}^{vib} and electronic free energy F_{mix}^{el}, which are not included in MC sampling. Although electronic contribution is typically small at room temperature, vibrational contribution may not be always negligible[43,44]. To understand the role of vibrational free energy on the relative stability of two types of SROs, we randomly choose representative configurations from MC trajectories and compute F_{mix}^{vib} by integrating the calculated phonon density of states through harmonic approximation (see "Methods"). As shown in Supplementary Table 2 and Supplementary Fig. 16, the difference in F_{mix}^{vib} between R-SRO and E-SRO is found to be less than 0.2 meV/atom, indicating that F_{mix}^{vib} is nearly independent of the degree of ordering, thus dose not affect the relative stability of SRO structures.

Impact on electronic band structures. The occurrence of SRO has been shown to substantially affect the band gaps in both GeSn[12] and SiSn[13] alloys. In light of the greater variation in alloy's structures due to different SROs in Si–Ge–Sn alloys, a significant change in electronic structures is expected. To explore this, we compare the calculated band structures of $Si_{0.125}Ge_{0.625}Sn_{0.25}$ alloy with a random distribution, R-SRO, and E-SRO. As shown in Fig. 4, the calculated band structures display salient distinctions among the three types of structures. A random alloy is found to exhibit a direct band gap at Γ, with the magnitude of ~0.25 eV. With R-SRO, the gap is found to increase to
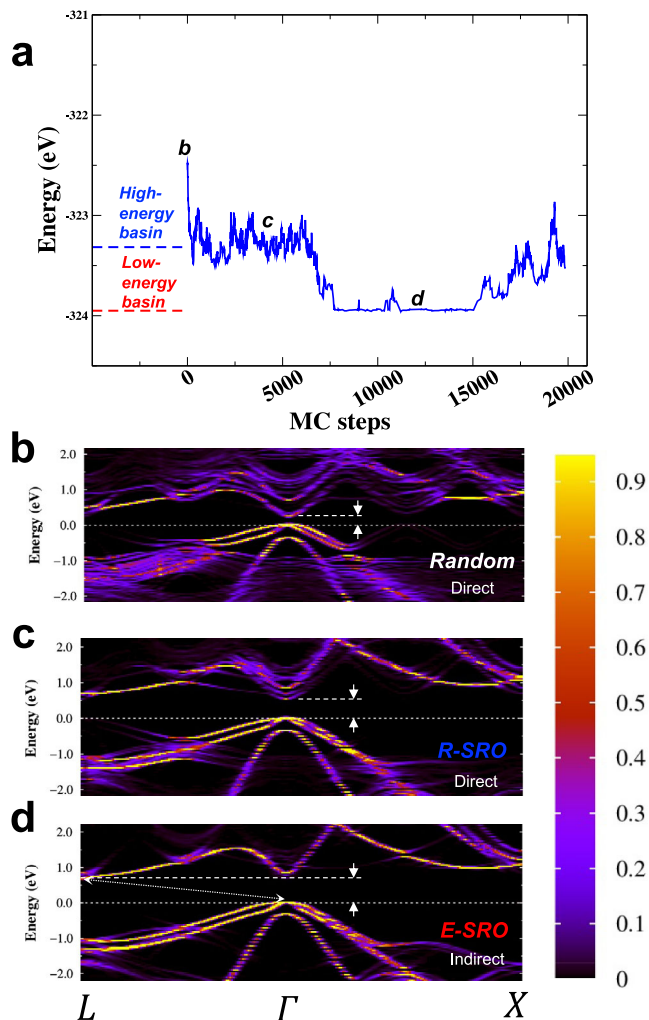
Fig. 4 Variation of the calculated electronic band structure with SRO in Si$_{0.125}$Ge$_{0.625}$Sn$_{0.25}$. a Configurations **b**–**d** are extracted from Monte Carlo trajectory 4 (see Fig. 1c). **b** A random distribution leads to a direct band gap at Γ of 0.25 eV. With R-SRO (**c**), the direct band is found to increase to 0.5 eV. **d** Further ordering through E-SRO yields an indirect band gap of ~0.75 eV, defined by a transition between Γ and L. Band structures of alloy are calculated by unfolding the wavefunction obtained from a 128-atom cell (see "Methods") to recover the Bloch character of electronic eigenstates in the Brillouin zone of a diamond cubic lattice. The corresponding Bloch spectral weight is color coded in the bar on the right.

~0.5 eV, while maintaining the direct character. Remarkably, when alloy adopts E-SRO, the direct gap at Γ sees a further significant increase so that the conduction band minimum at Γ is slightly above that at L, thus turning the band gap into an indirect type. The corresponding indirect band gap is ~0.75 eV. This significant change in band gaps and band characters thus highlights the substantial role of alloy structure, particularly the degree of SRO, plays in the optoelectronic properties of group IV alloys.

Discussion

The co-occurrence of R-SRO and E-SRO observed in our modeling study, along with the analysis showing their nearly degenerate thermodynamic stability, thus may well indicate a co-existence of both types of SROs in real Si–Ge–Sn MEAs. Since a dynamic transition between the two SROs requires re-

arrangement of atoms in the lattice, which can be kinetically prohibited at room temperature, such co-existence is more likely to bear a static form. One possible scenario for static co-existence is that Si–Ge–Sn MEAs are composed of iso-compositional domains with different degrees of SRO. Although the sizes of these domains are unclear, they are expected to be significantly smaller than a typical grain, and possibly around nanoscale, because the interface separating different SRO domains does not involve energetically unfavorable structures such as crystalline defects, thus the interfacial free energy is expected to be low. Consequently, Si–Ge–Sn alloys at equilibrium are expected to be structurally and spatially inhomogeneous at the *microscopic* level, albeit being macroscopically homogeneous and isotropic.

Regardless of its spatial distribution, the identified co-existence of two types of SROs has significant implications on the optoelectronic properties of Si–Ge–Sn alloys. First, the prediction of the key optoelectronic properties of Si–Ge–Sn alloy, e.g., band gap, type of band gap, critical compositions for indirect-to-direct transition, must take into account the significant role of SRO. We note that in III–V semiconductors which were discovered to exhibit a long-range, CuPt-type ordering, the role of ordering on optoelectronic properties has been extensively studied[45]. In contrast, there is a lack of similar understanding in group IV alloys. Given the large difference in the calculated band gap (~0.5 eV) between a random and E-SRO model for Si$_{0.125}$Ge$_{0.625}$Sn$_{0.25}$, it is highly likely that a prediction based on a random structure model may substantially underestimate the band gap. This has already been shown in GeSn[12] and SiSn[13] alloys, but is expected to be even more significant in ternary alloys. Certainly, such underestimate may become small or even negligible for a low Sn composition[46], where SRO becomes less prominent. However, since the projected line of composition for indirect-to-direct transition and the predicted constant bandgap contours for mid-infrared wavelength in Si–Ge–Sn alloys[42] cover high Sn content (see Supplementary Fig. 4) and significantly overlap the composition range where the co-existence of two SROs is clearly identified, a subsequent revisit to the current model is deemed necessary. Second, the measured optoelectronic properties of Si–Ge–Sn alloys reflect an ensemble average over all the contributions from the different structures with various degrees of SRO. Given the large variation in the electronic structures of SRO with different degrees that can co-exist, an averaged property *alone*, e.g., band gap, may not be sufficient to characterize alloy's optoelectronic properties. For example, Si–Ge–Sn alloys may exhibit smeared band edges, analogous to band tails in heavily doped semiconductors[47], instead of a rather abrupt, step-like onset of absorption coefficient as in a compound semiconductor. Such optoelectronic properties may affect the performance of the alloys, depending on exact types of potential applications. Third, the significant variation in electronic structure, which is solely due to the change in SRO, may also present an opportunity for band engineering. A critical limitation in combining two dissimilar band structures to create a heterojunction, e.g., quantum well, is the lattice mismatch between two different materials, which stands as one of the key challenges in epitaxial growth[48]. In this regard, a heterojunction composed of Si–Ge–Sn alloys with identical composition but different SROs, for example, R-SRO and E-SRO, can be advantageous, because the lattice constant of Si–Ge–Sn alloys only displays a very weak dependence on ordering (see Supplementary Table 3). Therefore, different types heterojunctions with tunable band offset may be potentially formed on demand through controlling SRO, not subject to the limitation due to lattice mismatch. Such band engineering strategy requires a control over the degree and type of SRO. We note that such control may be potentially achieved through tuning temperature in either growth or post-annealing, since the

entropic part of free energy explicitly depends on temperature. As a result, the free energy landscape of SRO can be effectively modified by temperature to shift both the average degree of SRO and the balance of coexistence. In particular, a higher temperature is expected to reduce the fraction of E-SRO, leading to a structure dominated by R-SRO, while a lower temperature will do the opposite. Indeed, SRO is being exploited to fine tune the mechanical properties in MEA and HEA metallic alloys[2,11,49].

Lastly, and perhaps even more importantly, it is expected that the observed phenomenon can exist generally in many other alloys. The co-existence of the two SROs is essentially due to the subtle balance between the enthalpy gain and the entropy loss upon an enhanced ordering of alloy configurations. Certainly, such balance cannot be always expected in any alloy, thus the discovery of the co-existence of two SROs in Si–Ge–Sn MEAs can be a fortunate case in this sense. However, we note that as the number of alloying elements increases, the configurational space of alloy increases combinatorially. As a consequence, both the energy landscape and free energy landscape become inevitably more complex. Therefore it is increasingly likely that there exist multiple local free energy minima with comparable stability in the SRO-parameter space. If this were true, multiple forms of SRO could emerge at equilibrium. These forms of SRO can be reflected by different combinations of various neighbors within the first few atomic shells that are nearly equally favorable over a random distribution. As a consequence, these alloys can be intrinsically heterogeneous in nanoscale, which has profound implications on the mechanical, optoelectronic, and thermal transport properties. In this regard, we note that MEA and HEA are very probable alloy systems to potentially exhibit this type of behavior. In fact, some of the very recent studies have already provided the sign for this. For example, a theoretical study on CoCuFeNiPd HEA[19] has demonstrated that SRO induces a composite structure consisting of three different types of clusters. Experimental characterization work has also observed concentration waves at nanoscale in both CrFeCoNiPd HEA[49] and VCoNi MEA[8]. Therefore, we expect more discoveries to follow as SRO in MEA and HEA is being intensively investigated.

Methods

Monte Carlo (MC) sampling. The Metropolis Monte Carlo (MC) method[50] is used to obtain the ensemble averages accounting for SRO, where the acceptance probability for a new configuration j generated from a trial move in configuration i equals to $\min\{1, \exp(-(E_j - E_i)/k_B T)\}$, where E_i and E_j are the total energies of configuration i and j, respectively, k_B is the Boltzmann constant, and T is temperature (300 K in this study). Each trial move (MC step) involves randomly selecting and swapping a pair of two atoms of different species to create a new configuration j, which then undergoes a full relaxation to obtain its energy E_j.

DFT calculations. Our density functional theory (DFT) calculations were performed with Vienna ab initio simulation package (VASP)[51] based on the projector augmented wave method[52–54]. Local density approximation (LDA)[55] was employed for the exchange-correlation functional, which has been shown to yield the best agreement with experiment on pure Ge and Sn for geometry optimization[56–59]. Different exchange correlation functionals were found to lead to comparable energy differences, which is of central importance to MC sampling (see Supplementary Fig. 17). As the number of configurations increases combinatorially with the number of atoms, a simulation cell containing 64 atoms, obtained by replicating a conventional diamond cubic (DC) cell containing eight atoms twice along each dimension, is chosen to ensure a sufficient sampling at the DFT level is feasible. We note that such system size is sufficiently large to accurately describe the energies of the key structural units pertaining to SRO in Si–Ge–Sn alloys, as validated through tests using larger cells (see Supplementary Note 1 for more details). For a 64-atom cell, we used $2 \times 2 \times 2$ Monkhorst-Pack k-points grid[60] with a plane-wave cutoff energy of 300 eV. Each new configuration undergoes full relaxation where both the cell geometry and atomic positions are relaxed. The conjugate-gradient algorithm is applied for structural relaxation during each energy calculation, with the convergence criteria of 10^{-4} eV and 10^{-3} eV for electronic and ionic relaxations, respectively. To cross-validate the identified SRO structures against size and shape effects, we also carried out MC sampling based on

128-atom cells created by replicating the primitive cell of the DC structure four times along each dimension (see Supplementary Fig. 1). In this case, only gamma point is used to sample the Brillouin zone for higher computational efficiency. We note that the choice of all these parameters has been carefully examined to ensure the total energy difference between two configurations i and j ($\Delta E = E_j - E_i$), which plays a crucial role in MC sampling, is well converged.

SRO parameter. The SRO parameter α_{ij}^m is defined as

$$\alpha_{ij}^m = 1 - \frac{N_{ij}^m}{N_{0,ij}^m}, \qquad (1)$$

where $N_{0,ij}^m$ and N_{ij}^m are the numbers of pairs between element i and j in the mth coordination shell for a random distribution and the actual distribution, respectively. By definition, a random distribution yields $\alpha_{ij}^m = 0$. $0 < \alpha_{ij}^m \le 1$ indicates a depletion of i, j pairs, with $\alpha_{ij}^m = 1$ meaning a complete depletion, while $\alpha_{ij}^m < 0$ suggests a preference of i, j pairs. Note that α_{ij}^m is different from but related to the commonly adopted Warren–Cowley SRO parameter[1].

Quasi-chemical approximation. The configuration entropy of mixing ΔS_{mix}^{con} is estimated based on the extension of quasi-chemical approximation[40] from binary alloys to multi-component alloys. For ternary system composed of species A, B, and C with composition of x_A, x_B, and x_C, the configuration entropy per atom can be approximated by

$$\Delta S_{mix}^{con} = -k_B \left[\sum_{i=A,B,C} x_i \ln x_i + \sum_j \left(x_j \ln x_j - x_j \ln x_j^0 \right) \right], \qquad (2)$$

where k_B is the Boltzmann constant, x_i is the concentration of species i, x_j^0 is the concentration of the micro-cluster j in the random solution model, and x_j is the concentration of the cluster j in the real solution modeled by MC sampling through taking SRO into account. Given the deviation of first-nearest-neighbor pair (Fig. 2 and Supplementary Fig. 2) and triplets (Supplementary Fig. 3) from random solution due to SRO, here we choose triplets as micro-clusters to estimate configurational entropy, which enables characterizing SRO through both triplets and first-nearest-neighbor pairs (embedded as constituents of triplets).

Band structure calculations. For band structure calculations, we employ the modified Becke–Johnson (mBJ) exchange potential[59], as implemented in VASP code, with the c-mBJ parameter set to be 1.2, which has been demonstrated to predict the correct band gaps of Si, Ge and α-Sn, in good agreement with experimental data and much computationally efficient than hybrid functionals or GW methods[56,57,59]. We apply the spectral weight approach[61,62] to unfold the band structures back into the first primitive Brillouin Zone of DC structure using the code fold2bloch[62]. Since the spectral weight approach as implemented in fold2bloch[62] requires the supercells built on the basis of primitive cells instead of conventional ones, band structure calculations are carried out on 128-atom supercells transformed from the 64-atom supercells generated from the MC/DFT trajectories, with a transformation matrix $[[0, 1, 1], [1, 0, 1], [1, 1, 0]]$. Relativistic effects (spin–orbit coupling) are included in the band structure calculation, which has been demonstrated to be crucial for reproducing the band structures of Ge and α-Sn[56,57].

Vibrational Helmholtz free entropy calculations. Vibrational Helmholtz free energy F_{mix}^{vib} is calculated through the harmonic approximation[63], using the phonopy code[64] interfaced with VASP. For Si–Ge–Sn alloy, we compute the second-order interatomic force constants using the finite-displacement method with an atomic displacement of 0.01 Å in supercells containing 512 atoms, duplicated $2 \times 2 \times 2$ from the 64-atom supercells generated from the MC/DFT trajectories, using the Γ-point sampling for electronic self-consistent calculations. For pure Si, Ge, and α-Sn, we used supercells containing 128 atoms, duplicated $4 \times 4 \times 4$ from the optimized primitive unit cells, with $2 \times 2 \times 2$ k-points for electronic self-consistent calculations. The post-processing of the results was performed with the phonopy code[64]. The convergence is carefully checked with the q-points meshes up to $8 \times 8 \times 8$ for Si–Ge–Sn alloy and $35 \times 35 \times 35$ for pure Si, Ge, and α-Sn. An energy convergence threshold of 10^{-8} eV was used in the calculations.

Data availability

The data that support the findings of this study are available from the corresponding author upon reasonable request.

Code availability

The MC code that is used in this study is available from the corresponding author upon reasonable request.

References

1. Cowley, J. M. An approximate theory of order in alloys. *Phys. Rev.* **77**, 669–675 (1950).
2. Zhang, R. et al. Short-range order and its impact on the CrCoNi medium-entropy alloy. *Nature* **581**, 283–287 (2020).
3. Wu, Y. et al. Short-range ordering and its effects on mechanical properties of high-entropy alloys. *J. Mater. Sci. Technol.* **62**, 214–220 (2021).
4. Jiang, B. et al. High-entropy-stabilized chalcogenides with high thermoelectric performance. *Science* **371**, 830–834 (2021).
5. Roychowdhury, S. et al. Enhanced atomic ordering leads to high thermoelectric performance in AgSbTe$_2$. *Science* **371**, 722–727 (2021).
6. Ji, H. et al. Hidden structural and chemical order controls lithium transport in cation-disordered oxides for rechargeable batteries. *Nat. Commun.* **10**, 592 (2019).
7. Zhang, R. et al. Direct imaging of short-range order and its impact on deformation in Ti-6Al. *Sci. Adv.* **5**, eaax2799 (2019).
8. Chen, X. et al. Direct observation of chemical short-range order in a medium-entropy alloy. *Nature* **592**, 712–716 (2021).
9. Tamm, A., Aabloo, A., Klintenberg, M., Stocks, M. & Caro, A. Atomic-scale properties of Ni-based FCC ternary, and quaternary alloys. *Acta Mater.* **99**, 307–312 (2015).
10. Singh, P., Smirnov, A. V. & Johnson, D. D. Atomic short-range order and incipient long-range order in high-entropy alloys. *Phys. Rev. B* **91**, 224204 (2015).
11. Ding, J., Yu, Q., Asta, M. & Ritchie, R. O. Tunable stacking fault energies by tailoring local chemical order in CrCoNi medium-entropy alloys. *Proc. Natl Acad. Sci. USA* **115**, 8919–8924 (2018).
12. Cao, B., Chen, S., Jin, X., Liu, J. & Li, T. Short-range order in GeSn alloy. *ACS Appl. Mater. Interfaces* **12**, 57245–57253 (2020).
13. Jin, X., Chen, S. & Li, T. Short-range order in SiSn alloy enriched by second-nearest-neighbor repulsion. *Phys. Rev. Mater.* **5**, 104606 (2021).
14. Fernandez-Caballero, A., Wrobel, J. S., Mummery, P. M. & Nguyen-Manh, D. Short-range order in high entropy alloys: Theoretical formulation and application to Mo-Nb-Ta-V-W system. *J. Phase Equilibria Diffusion* **38**, 391–403 (2017).
15. Feng, W., Qi, Y. & Wang, S. Effects of short-range order on the magnetic and mechanical properties of FeCoNi(AlSi)$_x$ high entropy alloys. *Metals* **7**, 482 (2017).
16. Kostiuchenko, T., Ruban, A. V., Neugebauer, J., Shapeev, A. & Kormann, F. Short-range order in face-centered cubic VCoNi alloys. *Phys. Rev. Mater.* **4**, 113802 (2020).
17. Chen, S. et al. Chemical-affinity disparity and exclusivity drive atomic segregation, short-range ordering, and cluster formation in high-entropy alloys. *Acta Mater.* **206**, 116638 (2021).
18. Li, Q.-J., Sheng, H. & Ma, E. Strengthening in multi-principal element alloys with local-chemical-order roughened dislocation pathways. *Nat. Commun.* **10**, 3563 (2019).
19. Chen, S. et al. Simultaneously enhancing the ultimate strength and ductility of high-entropy alloys via short-range ordering. *Nat. Commun.* **12**, 4953 (2021).
20. Soref, R. A. & Perry, C. H. Predicted band gap of the new semiconductor SiGeSn. *J. Appl. Phys.* **69**, 539–541 (1991).
21. Gencarelli, F. et al. Crystalline properties and strain relaxation mechanism of CVD grown GeSn. *ECS J. Solid State Sci. Technol.* **2**, P134 (2013).
22. Wirths, S., Buca, D. & Mantl, S. Si alloys: From growth to applications. *Prog. Crystal Growth Characterization Mater.* **62**, 1–39 (2016).
23. Ghetmiri, S. A. et al. Direct-bandgap GeSn grown on silicon with 2230 nm photoluminescence. *Appl. Phys. Lett.* **105**, 151109 (2014).
24. Wirths, S. et al. Lasing in direct-bandgap GeSn alloy grown on Si. *Nat. Photonics* **9**, 88–92 (2015).
25. Stange, D. et al. Optically pumped GeSn microdisk lasers on Si. *ACS Photonics* **3**, 1279–1285 (2016).
26. Reboud, V. et al. Optically pumped GeSn micro-disks with 16% Sn lasing at 3.1 μm up to 180 K. *Appl. Phys. Lett.* **111**, 092101 (2017).
27. Al-Kabi, S. et al. An optically pumped 2.5 μm GeSn laser on Si operating at 110 K. *Appl. Phys. Lett.* **109**, 171105 (2016).
28. Margetis, J. et al. Si-based GeSn lasers with wavelength coverage of 2 μm and operating temperatures up to 180 K. *ACS Photonics* **5**, 827–833 (2018).
29. Dou, W. et al. Optically pumped lasing at 3 μm from compositionally graded GeSn with tin up to 22.3%. *Opt. Lett.* **43**, 4558–4561 (2018).
30. Kurosawa, M. et al. Near-infrared light absorption by polycrystalline SiSn alloys grown on insulating layers. *Appl. Phys. Lett.* **106**, 171908 (2015).
31. Tolle, J. et al. Low temperature chemical vapor deposition of Si-based compounds via SiH$_3$SiH$_2$SiH$_3$: Metastable SiSn/GeSn/Si(100) heteroepitaxial structures. *Appl. Phys. Lett.* **89**, 231924 (2006).
32. McCarthy, T. T., Ju, Z., Schaefer, S., Yu, S.-Q. & Zhang, Y.-H. Momentum(k)-space carrier separation using SiGeSn alloys for photodetector applications. *J. Appl. Phys.* **130**, 223102 (2021).
33. Widom, M., Huhn, W. P., Maiti, S. & Steurer, W. Hybrid Monte Carlo/molecular dynamics simulation of a refractory metal high entropy alloy. *Metall. Mater. Trans. A* **45**, 196–200 (2014).
34. Hickman, J. & Mishin, Y. Temperature fluctuations in canonical systems: Insights from molecular dynamics simulations. *Phys. Rev. B* **94**, 184311 (2016).
35. Fleurial, J. P. & Borshchevsky, A. Si–Ge–metal ternary phase diagram calculations. *J. Electrochem. Soc.* **137**, 2928–2937 (1990).
36. Moody, M. P. et al. Atomically resolved tomography to directly inform simulations for structure-property relationships. *Nat. Commun.* **5**, 1–10 (2014).
37. Zhang, F. et al. Local structure and short-range order in a NiCoCr solid solution alloy. *Phys. Rev. Lett.* **118**, 205501 (2017).
38. Mukherjee, S. et al. Short-range atomic ordering in nonequilibrium silicon-germanium-tin semiconductors. *Phys. Rev. B* **95**, 161402 (2017).
39. Shimura, Y. et al. EXAFS study of local structure contributing to Sn stability in Si$_y$Ge$_{1-y-z}$Sn$_z$. *Mater. Sci. Semicond. Process.* **70**, 133–138 (2017).
40. Sher, A., Schilfgaarde, M. V., Chen, A.-B. & Chen, W. Quasichemical approximation in binary alloys. *Phys. Rev. B* **36**, 4279–4295 (1987).
41. Xu, C. et al. Synthesis and fundamental studies of Si-compatible (Si)GeSn and GeSn mid-IR systems with ultrahigh Sn contents. *Chem. Mater.* **31**, 9831–9842 (2019).
42. Moutanabbir, O. et al. Monolithic infrared silicon photonics: The rise of (Si) GeSn semiconductors. *Appl. Phys. Lett.* **118**, 110502 (2021).
43. Manzoor, A., Pandey, S., Chakraborty, D., Phillpot, S. R. & Aidhy, D. S. Entropy contributions to phase stability in binary random solid solutions. *npj Comput. Mater.* **4**, 1–10 (2018).
44. Esters, M. et al. Settling the matter of the role of vibrations in the stability of high-entropy carbides. *Nat. Commun.* **12**, 5747 (2021).
45. Mascarenhas, A. (ed) *Spontaneous Ordering in Semiconductor Alloys* (Springer Science & Business Media, 2002).
46. Pearce, P. M., Broderick, C. A., Nielsen, M. P., Johnson, A. D. & Ekins-Daukes, N. J. Electronic and optical properties of Si$_x$Ge$_{1-x-y}$Sn$_y$ alloys lattice-matched to Ge. *Physical Review Materials* **6**, 015402 (2022).
47. Mieghem, P. V. Theory of band tails in heavily doped semiconductors. *Rev. Mod. Phys.* **64**, 755–793 (1992).
48. Moutanabbir, O. & Gosele, U. Heterogeneous integration of compound semiconductors. *Annu. Rev. Mater. Res.* **40**, 469–500 (2010).
49. Ding, Q. et al. Tuning element distribution, structure, and properties by composition in high-entropy alloys. *Nature* **574**, 223–227 (2019).
50. Metropolis, N., Rosenbluth, A. W., Rosenbluth, M. N., Teller, A. H. & Teller, E. Equation of state calculations by fast computing machines. *J. Chem. Phys.* **21**, 1087–1092 (1953).
51. Kresse, G. & Hafner, J. Ab initio molecular dynamics for liquid metals. *Phys. Rev. B* **47**, 558–561 (1993).
52. Kresse, G. & Joubert, D. From ultrasoft pseudopotentials to the projector augmented-wave method. *Phys. Rev. B* **59**, 1758–1775 (1999).
53. Kresse, G. & Furthmuller, J. Efficiency of ab-initio total energy calculations for metals and semiconductors using a plane-wave basis set. *Comput. Mater. Sci.* **6**, 15–50 (1996).
54. Kresse, G. & Furthmuller, J. Efficient iterative schemes for ab initio total-energy calculations using a plane-wave basis set. *Phys. Rev. B* **54**, 11169–11186 (1996).
55. Ceperley, D. M. & Alder, B. J. Ground state of the electron gas by a stochastic method. *Phys. Rev. Lett.* **45**, 566–569 (1980).
56. Eckhardt, C., Hummer, K. & Kresse, G. Indirect-to-direct gap transition in strained and unstrained Sn$_x$Ge$_{1-x}$ alloys. *Phys. Rev. B* **89**, 165201 (2014).
57. Polak, M. P., Scharoch, P. & Kudrawiec, R. The electronic band structure of Ge$_{1-x}$Sn$_x$ in the full composition range: Indirect, direct, and inverted gaps regimes, band offsets, and the Burstein effect. *J. Phys. D: Appl. Phys.* **50**, 195103 (2017).
58. Haas, P., Tran, F. & Blaha, P. Calculation of the lattice constant of solids with semilocal functionals. *Phys. Rev. B* **79**, 085104 (2009).
59. Tran, F. & Blaha, P. Accurate band gaps of semiconductors and insulators with a semilocal exchange-correlation potential. *Phys. Rev. Lett.* **102**, 226401 (2009).
60. Monkhorst, H. J. & Pack, J. D. Special points for Brillouin-zone integrations. *Phys. Rev. B* **13**, 5188 (1976).
61. Popescu, V. & Zunger, A. Effective band structure of random alloys. *Phys. Rev. Lett.* **104**, 236403 (2010).

62. Rubel, O., Bokhanchuk, A., Ahmed, S. J. & Assmann, E. Unfolding the band structure of disordered solids: From bound states to high-mobility Kane fermions. *Phys. Rev. B* **90**, 115202 (2014).

63. Dove, M. T. *Introduction to Lattice Dynamics. Cambridge Topics in Mineral Physics and Chemistry* (Cambridge University Press, 1993).

64. Togo, A. & Tanaka, I. First principles phonon calculations in materials science. *Scr. Mater.* **108**, 1–5 (2015).

Author contributions

T.L. conceived and supervised the research, X.J. and T.L. performed the MC simulations, S.C. performed electronic band structures calculations and vibrational properties calculations, X.J., S.C., and T.L. analyzed the results, X.J. and S.C. performed the validation. All authors contributed to the writing of the manuscript.

Competing interests

The authors declare no competing interests.

Additional information

Supplementary information The online version contains supplementary material available at https://doi.org/10.1038/s43246-022-00289-5.

Correspondence and requests for materials should be addressed to Tianshu Li.

Peer review information *Communications Materials* thanks Shuai Chen and the other, anonymous, reviewer(s) for their contribution to the peer review of this work. Primary Handling Editor: John Plummer.

Reprints and permission information is available at http://www.nature.com/reprints

Publisher's note Springer Nature remains neutral with regard to jurisdictional claims in published maps and institutional affiliations.